Magnetic Resonance Microscopy Analysis of Advective Transport in a Biofilm Reactor

Erica L. Gjersing, Sarah L. Codd, Joseph D. Seymour, Philip S. Stewart

Department of Chemical and Biological Engineering and Center for Biofilm Engineering, Montana State University, 306 Cobleigh Hall, PO Box 173920, Bozeman, Montana 59717-3920; telephone: 406-994-6853; fax: 406-994-5308; e-mail: jseymour@coe.montana.edu

Received 5 August 2004; accepted 5 November 2004

Published online 4 February 2005 in Wiley InterScience (www.interscience.wiley.com). DOI: 10.1002/bit.20400

Abstract: In this article we present magnetic resonance microscopy (MRM) characterization of the advective transport in a biofilm capillary reactor. The biofilm generates non-axial flows that are up to 20% of the maximum axial velocity. The presence of secondary velocities of this magnitude alters the mass transport in the bioreactor relative to non-biofilm fouled reactors and questions the applicability of empirical mass transfer coefficient approaches. The data are discussed in the context of simulations and models of biofilm transport and conceptual aspects of transport modeling in complex flows are also discussed. The variation in the residence time distribution due to biofilm growth is calculated from the measured propagator of the motion. Dynamical systems methods applied to model fluid mixing in complex flows are indicated as a template for extending mass transport theory to quantitatively incorporate microscale data on the advection field into macroscale mass transfer models. © 2005 Wiley Periodicals, Inc.

Keywords: magnetic resonance imaging; biofilm; transport; residence time distribution

INTRODUCTION

The biofilm-forming bacterium *Staphylococcus epidermidis* has been implicated in many medical implant infections. It is normal flora on the skin of humans, so any device that comes in contact with skin has the possibility of becoming infected. Mechanical heart valves, shunts, catheters, and orthopedic devices are some examples of implanted devices which are commonly infected by *S. epidermidis* biofilms (Costerton et al., 1999). Once infected, a patient often must undergo surgery to remove and replace the implant since antibiotics are less effectual at eradicating biofilms (Stewart and Costerton, 2001). Biofilms which grow on implants such as mechanical heart valves are continuously subjected to high flow rates, which cause the biofilm structure to develop high tensile strength (Hyde et al., 1998). The fluid surrounding a biofilm controls growth in that it provides the primary source of nutrients, facilitates the removal of cell by-products and is the vehicle for biocide delivery. Quantifying how biofilms interact with bulk fluid flow, or advection, around them is critical to modeling mass transport in biofilm systems (Beyenal and Lewandowski, 2002), shear stress influences on structure of biofilms (Stoodley et al., 1999a) and detachment rates (Picioreanu et al., 2000a).

Measuring spatial distributions of velocity within bioreactors has historically been difficult, in part due to biofilm opacity. Particle tracking, where microscopic fluorescent spheres are tracked with confocal laser microscopy, is time- and labor-intensive and measures a tracer response to the flow (de Beer et al., 1994; Stoodley et al., 1994). This confocal particle tracking work has allowed researchers to study the fluid flow within interstitial voids of biofilms (de Beer et al., 1994) and combined with microelectrodes to calibrate limiting current density measurements and obtain fluid velocity distribution around clusters of biofilm (Xia et al., 1998). In systems where the velocity is of higher spatial dimension and/or time-dependent, streamlines and streaklines can diverge and a tracer measurement provides particle size-dependent Lagrangian tracking as opposed to the spatial distribution of the molecules composing the bulk flow field (Batchelor, 1967).

The research we present in this article applies magnetic resonance microscopy (MRM) to study the interaction between a biofilm and fluid dynamics in a capillary bioreactor. Magnetic resonance microscopy accurately and noninvasively images spatial distributions of velocity fields in biofilm systems (van As and Lens, 2001). Low-resolution images averaged over large slices of fluid flowing over a biofilm-fouled surface were first published in 1992 and showed the boundary layer impact on axial velocity in the presence of a biofilm (Lewandowski et al., 1992). Recently, images of fluid flowing through a circular biofilm-fouled capillary demonstrated the ability of MRM to image the axial flow and calculate shear force on the biofilm surface as a function of the 2D capillary cross-section (Manz et al., 2003). Magnetic resonance microscopy measurement of 3D components of velocity as a function of 2D spatial distri-

Correspondence to: Joseph D. Seymour

Contract grant sponsors: W.M. Keck Foundation; the Office of Science (BER) U.S. Department of Energy; the National Science Foundation; Donors of the American Chemical Society Petroleum Research Fund

Contract grant numbers: DE-FG02-03ER63576; DMI-0340709; CTS-0348076

bution in a square glass capillary fouled with biofilm indicate significant non-axial flows are generated by the biofilm (Seymour et al., 2004). In this article we present further research that correlates T_2 magnetic relaxation maps displaying biofilm structure with the corresponding velocity patterns in three dimensions in a biofilm-fouled square capillary. The bacterial species *Staphylococcus epidermidis* strain 35984 is studied in these experiments. This microbial species is chosen for its medical importance and the fact that it forms thick opaque biofilms, hundreds of microns thick, in a relatively short amount of time. Biofilms this thick are hard to study with optical methods like confocal laser microscopy because laser light cannot penetrate the biomass far enough to elucidate the innermost structures. Since molecular motions provide a spatial resolution limit of about 5 μm in standard MRM methods, thick biofilms are well suited to the technique. A square duct geometry is chosen to provide correlation with existing experiments and simulations, as research bioreactors tend to be of square or rectangular cross-section for optical or microelectrode access. The spatially resolved velocity data provide details on the impact of biofilm-induced advection on mass transport from the bulk fluid to the biofilm and through the capillary bioreactor. These issues are of significant importance in biosensor and bioseparations applications based on microfluidics or "lab on a chip" technology (Stone and Kim, 2001).

THEORY

Magnetic Resonance Microscopy (MRM)

Magnetic resonance microscopy (Callaghan, 1991) involves the use of strong three-dimensional magnetic field gradients to investigate flow, diffusion, and magnetic relaxation in matter on scales of the order of 10 μm spatial resolution. Information obtained from molecular motions over the entire sample or within the spatial resolution provides data on spatial scales down to 10 nm over timescales ranging from 10 μs to 1s. Magnetic resonance imaging (MRI) is an indispensable clinical and research tool for physicians, most importantly because it allows non-invasive visualization of soft tissue in the body. Since the late 1980s laboratory images have been achieved with resolutions of 10 μm^3, across samples of $\approx$ 5 cm, hence the birth of a research area termed MR Microscopy (Callaghan, 1991). The use of the separate terms MRI and MRM is adopted in part to make clear that different hardware, and hence accessible sample sizes, are used in generating very high spatial resolution MRM data in contrast to the large bore clinical magnet systems associated with lower resolution MRI. Issues such as magnetic susceptibility effects at material interfaces and the scales of variation in samples require trade-offs in the best hardware configuration to study a specific problem.

Much of the potential of MRM lies not in its high resolution spin density maps, but rather in the non-invasive, non-destructive spatially resolved flexibilities utilizing a wide range of physical and chemical molecular scale contrast mechanisms (Callaghan, 1991). These capabilities have made MRM a premier technique in soft condensed matter studies of materials that are inaccessible to most imaging methods. The most obvious contrast mechanism is spin density, or molecular density, to which chemical shift techniques can be applied to selectively excite certain molecular species leading to the spatial mapping of a specific molecule. Alternatively, three-dimensional maps may be obtained where the pixel signal intensity is directly proportional to nuclear spin relaxation times (T_1, T_2, or $T_{1\rho}$). Relaxation times are related to the rotational and translational freedom of the molecule and most often used to distinguish more solid-like materials from more liquid-like materials, or to provide soft matter contrast when spin density is similar. The NMR signal may also be encoded for translational molecular motion and quantitative spatial maps of self-diffusion and velocity fields can be obtained.

As we show, these techniques have immense application to biofilm research. The physical or chemical environment of the sample can be altered significantly and any spatial variations that these conditions cause can be examined through observable changes in the molecular environment during growth. Designing the appropriate sequence often requires a great deal of expert knowledge, specialized hardware, and patience, and interpreting the results often involves close contact between experts researching the particular material and the MR microscopist. However, the potential to obtain otherwise inaccessible information makes the pursuit worthwhile for many biological materials problems.

Transverse Magnetic Relaxation Maps

The MRM pulse sequence used to "image" the biofilm is an adaptation of a basic spin-warp slice selection sequence where the spins in the slice of interest ($z = -s/2$ to $s/2$) are excited at an initial time with a 90° radio frequency (rf) pulse (Fig. 1a; Callaghan, 1991). Gradients in the x and y direction are stepped through such that for each gradient value the spins acquire a magnetization phase shift dependent on their location within that gradient. The signal is dephased and refocused at effective echo times of $1t_e$, $2t_e$, $3t_e \ldots 8t_e$ (Edzes et al., 1998). The MR signal, $S(k_x, k_y, t_e)$ obtained at each echo time is the Fourier inversion of the spin density, $\rho(x, y, z)$ weighted by the average relaxation time parameter $T_2(x, y, z)$ at each image voxel.

$$S(k_x, k_y, t_e) = \int_{-s/2}^{s/2} \left[\int_{-\infty}^{\infty} \int_{-\infty}^{\infty} [\exp\{-t_e/T_2(x,y,z)\}\rho(x,y,z)] \times \exp\{i2\pi k_x x + k_y y\} dx dy \right] dz \quad (1)$$

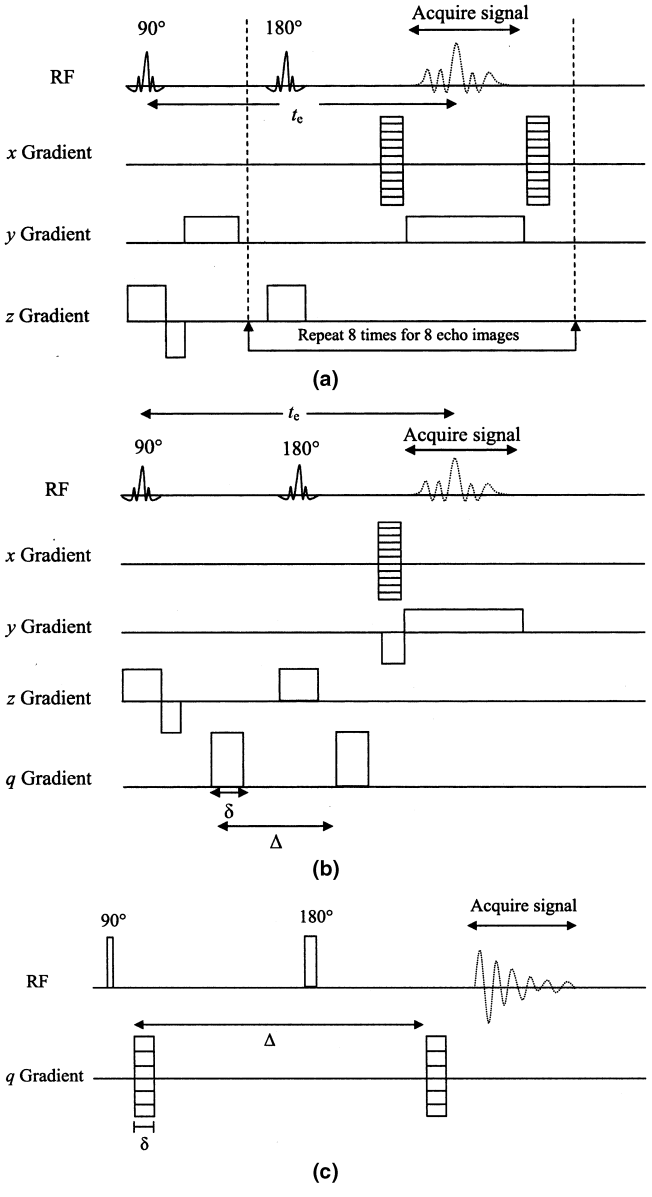

Figure 1. (a) Pulse sequence or timing diagram indicating the application of radio frequency excitation pulses and magnetic field gradients to generate a T_2 relaxation weighted image. To make a T_2 map the echo image is reproduced 8 times at different values of t_e. A map representing the decay rate of the signal in each image voxel distinguishes spins experiencing restricted motion in the biofilms, short T_2, from spins experiencing free diffusion in the bulk fluid, long T_2. (b) Velocity map pulse sequence. To make a velocity map the echo image is repeated with different values of the q gradient pulse. A velocity map is obtained by determining the phase shift at each image voxel due to the motion sensitizing effective bi-polar q-gradient and hence calculating the average displacement that occurred for those spins over the encoding time Δ. (c) Pulsed gradient spin echo pulse sequence for generation of the propagator, or conditional displacement probability $\bar{P}_s(Z, \Delta)$). The above sequence samples all of q space with positive and negative q values to obtain all the data points needed for the Fourier transform to construct artifact-free propagators.

where $k_i = (2\pi)^{-1}\gamma\, G_i\tau_i$, and τ_i is the duration of the gradient in the i-direction, G_i. Fourier transformation of the MR signal provides the relaxation weighted spin density $\rho(x, y)$ spatially averaged over the slice thickness in z and the gradients can be applied along any coordinate axis. The signal from spins in a restricted motion environment such as the biofilm will decay faster, shorter T_2, than signal from spins in free water, longer T_2, and a map of the average decay rate in each individual image pixel indicates where the biomass is located. This experimental sequence creates contrast maps in a time-efficient manner, however the T_2 values obtained are qualitative rather than quantitative.

Velocity Maps

The velocity maps are obtained using another adaptation of the basic spin-warp slice selection sequence, with a pair of gradient pulses added to encode for molecular motion (Callaghan, 1991). The pulses are located either side of the refocusing 180° pulse (Fig. 1b). The first gradient pulse encodes the spins with a phase in the magnetization dependent on their location at that point in time, and the second gradient pulse reverses this phase encoding. If a spin moves in the time period Δ, the spin retains a residual phase shift directly proportional to the displacement that has occurred in the time interval Δ. The MR spin echo signal normalized to eliminate relaxation effects, $E(k_x, k_y, q) = S(k_x, k_y, q)/S(k_x, k_y, q = 0)$, is the Fourier inversion of the density of the spins weighted by the coherent motion

$$E(k_x, k_y, q_i) = \int_{-s/2}^{s/2} \left[\int_{-\infty}^{\infty} \int_{-\infty}^{\infty} [\exp\{-i2\pi\Delta q_i v_i(x, y, z)\}\rho(x, y, z)] \times \exp\{i2\pi(k_x x + k_y y\}dxdy \right] dz \quad (2)$$

where $q_i = (2\pi)^{-1}\gamma g_i\delta$, and δ is the duration of the velocity encoding gradient applied in the i-direction, g_i. A map of the residual phase shift at each spatial location can then be interpreted as an image of the average velocity over time Δ in each image pixel. Additional time averaging occurs as the velocity maps take approximately 10 minutes to acquire, so flow changes on a time scale shorter than this are averaged for each pixel providing the stationary velocity (Li et al., 1994).

Propagator [Conditional Displacement Probability P(Z, Δ)]

In the pulsed gradient spin echo sequence (Fig. 1c), only a pair of pulsed magnetic field gradients are applied so as to encode in the phase of the magnetization the location of all MR active spins at an initial time and then unwind that phase at a set time Δ later, generating phase shifts dependent on molecular dynamics over time Δ, from the entire sample. No spatially localized image data is obtained. The measured echo signal, $E(q, \Delta)$ is the Fourier

inversion of the propagator averaged over the initial spin density $\rho(z)$,

$$E(q) = \int_{-\infty}^{\infty} \bar{P}(Z, \Delta) \exp\{i2\pi qZ\} dZ \quad (3)$$

where $q = (2\pi)^{-1}\ \gamma g \delta$ is the Fourier reciprocal wavelength to displacement $Z = z' - z$ and $\bar{P}(Z, \Delta)$ the averaged propagator (Callaghan, 1991). This allows a statistical measurement of the fine details of the dynamics over the entire sample to be obtained. The function can also be discussed in terms of the probability distribution of velocities for times Δ short relative to the time scale over which variations in velocity occur $\bar{P}(Z, \Delta) \equiv \bar{P}(v_z) = \bar{P}(Z, \Delta)$ (Callaghan et al., 1999; Garroway, 1974).

Transport in Capillary Bioreactors

Biofilms adhere to surfaces, hence in nearly all systems of interest, whether a medical device or geological media, transport of mass from bulk fluid to the biofilm–fluid interface is impacted by the velocity field (Eberl et al., 2000; Stoodley et al., 1997). Since the bulk fluid velocity controls the shear stress imparted to the biofilm and fluctuations in shear stress have been measured (Stoodley et al., 1999b) there is potential for the velocity to impact mass transport within the biofilm by generating compression induced variations in the extracellular polymeric substance (EPS) hydrogel structure. The coupling of the velocity field to mass transport is a fundamental aspect of mass conservation (Bird et al., 2002). The concentration of a species, $c(\mathbf{r}, t)$, satisfies the advection diffusion equation

$$\underbrace{\frac{\partial c}{\partial t}}_{\text{rate of change of mass}} + \underbrace{\nabla \cdot (\mathbf{v}c)}_{\text{flux by advection}} = \underbrace{\nabla \cdot \mathbf{D} \cdot \nabla c}_{\text{flux by diffusion}} + \underbrace{R}_{\text{rate of mass consumption or production}} \quad (4)$$

The spatial and temporal evolution of the concentration field is dependent on the velocity field vector $\mathbf{v}(\mathbf{r}, t)$, the diffusion tensor $\mathbf{D}(\mathbf{r}, t)$ and any reactions occurring in the system $R(\mathbf{r}, t)$. Non-dimensionalization of Eq. (4) generates the Peclet number, $Pe = v_{z,\max} l/D$, which multiplies the left-hand side indicating the ratio of advective to diffusive mass transport (Bird et al., 2002). In capillary systems for $Re <$ 2000 flow is considered laminar and only the axial component of the velocity vector is present and it is rectilinear, $\mathbf{v} = (0,0, v_z(x, y))$. In turbulent flow with $Re >$ 2000 or flows that exhibit hydrodynamic instabilities $\mathbf{v} = (v_x(x, y, z), v_y(x, y, z), v_z(x, y, z))$.

The modeling of mass transport from bulk fluid to interface in capillary flow typically applies an empirical mass transfer coefficient approach. In a non-reactive steady-state laminar flow in a square conduit with constant molecular diffusion D the mass balance in the fluid takes the form

$$0 = -v_z(x, y)\frac{\partial c(x, y, z)}{\partial z} + D\left(\frac{\partial^2 c(x, y, z)}{\partial x^2} + \frac{\partial^2 c(x, y, z)}{\partial y^2}\right) \quad (5)$$

indicating the direct mechanism for transport to the capillary surface is molecular diffusion and not advection (Lewandowski and Beyenal, 2003). Non-dimensionalization leads to, $Pe\ l/L = Pe_L\ l^2/L^2$, multiplying the advective term with the diffusive term of order 1 and the axial Peclet number, $Pe_L = v_{z,\max} L/D$, is naturally introduced. Mass transfer coefficient scaling relations for biofilm systems have been developed from both experiment (Beyenal and Lewandowski, 2002; Stoodley et al., 1997) and simulation (Eberl et al., 2000; Horn and Hempel, 1997; Picioreanu et al., 2000b). Correlations of the form $Sh \sim Re^{1/2}\ Sc^{1/2}$ (Horn and Hempel, 1997) and $Sh \sim Re^{1/3}\ Sc^{1/3}$ (Eberl et al., 2000) have been applied. Classically, the 1/2 power scaling is found analytically for boundary flow with fluid–fluid interfaces and no velocity gradient present at the interface, while 1/3 power scaling is found for fluid–solid interfaces with a velocity gradient at the interface (Bird et al., 2002). A limitation of mass transfer coefficient approaches is the inability to incorporate finer detail of the advection field into the correlation in a quantitative fashion. Of significant issue is the fact that in many low Re systems secondary flows with coherent structure, e.g., vortices, occur due to boundary-induced inertial effects and the mass transport is altered by the presence of bulk advection in the x- and y-directions (Picioreanu et al., 2000b), an issue studied extensively in the analysis of fluid mixing (Ottino, 1989).

The quantitative dependence of mass transport on fluid mixing is an open research question and the concepts of dynamical systems theory have been applied to characterize complex advection in mixing devices (Liechtenberg and Lieberman, 1992; Ottino, 1989, 1990). Qualitatively two effects can occur. The secondary flows can increase homogenization, so the concentration field is uniform and all points in the bulk fluid are near to the average bulk concentration. This situation leads to enhanced mass transport to the biofilm interface relative to a rectilinear flow since the region of diffusion limited transport and depleted concentration, i.e., hydrodynamic and concentration boundary layer, at the biofilm-fluid interface are decreased. Alternatively secondary flows can generate regions of fluid where regular motions inhibit exchange with the rest of the bulk fluid, creating a heterogeneous concentration distribution with regions of high and low concentration dependent on the structure of the advection field. The impact on mass transport is then conditional upon the interaction between the biofilm structure and the velocity distribution as to whether regions of high or low concentration are in contact with the interface. Lattice-Boltzmann simulations have clearly

elucidated these variations in local Sherwood number in heterogeneous biofilms (Picioreanu et al., 2000b).

In nonlinear mixing flows, dynamical systems simulations lead to a picture of the flow given by the Poincare section, the time repetition surface of fluid particle trajectories (Ottino, 1989). A mixing strength parameter based on the ratio of secondary to axial advection rate is used to characterize the flow, $\beta \sim (v_{x,\,\max}L)/(v_{z,\,\max}l)$ and the amount of chaotic motion increases with β (Ottino 1989). It is convenient to introduce a non-axial Peclet number, $Pe_l = v_{x(y),\,\max}\, l/D$, and an effective mixing strength can be expressed as $\beta \sim (Pe_l/Pe_L)(L/l)^2$. Mass transfer coefficient methods fail to characterize transport in these complex flows as they are unable to account for the structure of the velocity field and new methods for modeling, perhaps based on statistical mechanics methods are needed (Bouchaud and Georges, 1990).

One means of gaining quantitative information is using the residence time distribution (RTD) to determine the impact of advection field structures like vortices on the molecular transit time (Mezic et al., 1999; Ottino, 1989). The RTD quantifies the number of fluid particles which spend different durations in a reactor and is dependent upon the distribution of axial velocities, the time and spatial dependence of the mixing, and the reactor length (Fogler, 1986). Magnetic resonance microscopy measurements of the propagator of the motion for short observation times provide the velocity probability distribution and a simple relation between it and the RTD, $N(t)$ exists

$$N(L,t)dt = \tilde{P}(v_z)dv_z \tag{6}$$

This relation for connecting MRM data to the residence time distribution method does not appear to have been presented in the literature previously. Strictly speaking, the relationship in Eq. (6) only holds if there is no mixing or dispersion, i.e., if the velocity distribution remains constant for all observation times. However, the relationship provides insight since the RTD is an analysis method well understood in industrial situations and the propagator over time Δ can accurately describe the RTD for times on the order of Δ and within the timescale of mixing and dispersion events. It is important to note that an RTD depends on the length of the conduit analyzed, whereas the measured propagator depends on the observation time Δ of spin displacement evolution so the MRM measured residence time distributions provide scale-dependent analysis of the variation of the RTD with L varying up to the active region of the MRM coil.

MATERIALS AND METHODS

Biofilm Sample Preparation

The biofilms cultured for these experiments were grown in 1 mm square glass capillaries with gravity driven nutrient flow. The nutrient feed is 1/10th strength tryptic soy broth (DIFCO, Beckton Dickinson) at a volumetric flow rate of 0.028 mL s^{-1}, corresponding to an average velocity in a clean capillary of 28 mm s^{-1} with $Re = 90$. Note Re is calculated with $l = 1$ mm, since for a 1 mm square duct the hydraulic radius is 1 mm. After a no-flow inoculation period of 4 h to allow the suspended bacteria to settle and attach to the glass the biofilm is allowed to grow for 48 hours under these flow conditions. The biofilm sample is incubated at 37°C during all stages of the growth process to simulate human body temperature. After the 48-h growth period, the biofilm sample was then loaded into the magnet for study. The time-dependent growth data shown in Figure 2 are obtained using the same temperature and flow rate but with the bioreactor in the magnet 4 h after inoculation so that growth could be monitored.

Magnetic Resonance Microscopy Experiments

A Bruker Avance DRX spectrometer networked to a 250 MHz superconducting magnet was used to conduct the MRM experiments. Micro-imaging was accomplished using a Bruker Micro5 probe and gradient amplifiers to produce magnetic field gradients up to 2 T m^{-1}. A radio frequency (rf) coil with an internal diameter of 5 mm was used for all the NMR experiments presented. To acquire images and process diffusion and velocity data the Bruker imaging software package (Paravision) was employed. Additional data analysis to obtain velocity maps was performed using MatLab (MathWorks, Inc., Newton, MA). The medical contrast agent, Magnevist (Berlex Laboratories) was added to the feed at a concentration of 0.6 mL per liter nutrient feed to decrease the experiment times due to the decrease of the longitudinal relaxation time T_1. Magnevist will also decrease the transverse relaxation time, T_2, however the contrast between the bulk water and the biofilm material was not impacted, and the benefit to the SNR by the reduced T_1 time significantly enhanced the results. Low concentrations of Magnevist have been shown to have no affect on the growth of the biofilms (Lewandowski et al., 1992). Additionally, bacterial growth rate curves indicated no impact on the growth of planktonic bateria due to the presence of Magnevist.

The MRM measurements are of the ^1H protons on the H_2O molecules in the bulk fluid and within the biomass. T_2 maps are generated using a slice-selection 2D multi-spin echo imaging sequence (Fig. 1a) with the following parameter values: repetition time 500 ms, $t_e = 10$ ms, 8 echo images. Total acquisition time for each map was 5 minutes during which time the flow was stopped to enhance image resolution and avoid in-flow out-flow artifacts. Velocity data is acquired for flow at $Re = 32$, using a spin echo sequence with bi-polar velocity sensitizing gradients (Fig. 1b) with parameters of: repetition time 2000 ms, $t_e = 20$ ms, $g = 0$, and 100 mT/m, $\delta = 1$ ms, $\Delta = 7$ ms. The total acquisition time for the velocity maps, i.e., two images each

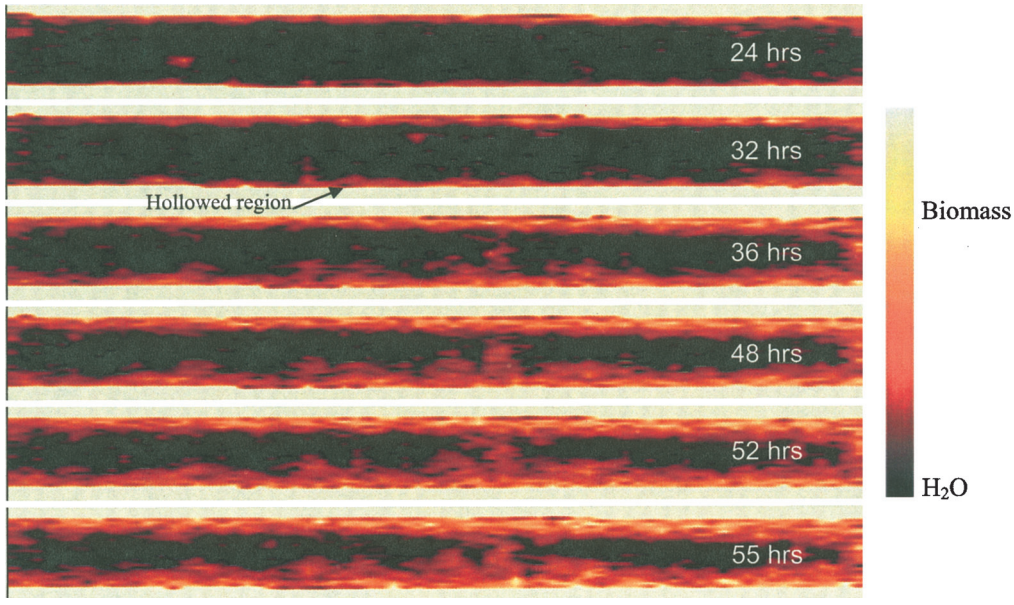

Figure 2. Time lapse T_2 maps of biofilms structure as a function of growth. The T_2 maps are collected at different stages in the growth of a biofilm at the time shown after initial inoculation. Orange tones indicate water restricted within a biofilm and black is the bulk unrestricted water. Images are acquired in the absence of flow, however, the flow direction for growth periods between images is left to right. The heterogeneity increases with growth. The T_2 maps represent a qualitative effective T_2 value and therefore the scale is represented as such. The average value in the biofilm was 40 ms and in the bulk water was 60 ms.

with different g value, is 17 minutes. The T_2 and velocity maps are averaged over a slice thickness of 0.3 mm with a field of view (FOV) of 2.5 mm × 20 mm over 64 × 128 pixels, for a spatial resolution of 39 × 156 μm/pixel.

RESULTS AND DISCUSSION

Time Evolution of Biofilm Structure

The ability of MRM to non-invasively monitor biofilms during growth provides the potential for extended studies of nutrient and biocide effects on biofilm structure and transport. Figure 2 demonstrates the capability to monitor biofilm structure in a capillary bioreactor over a 30-h period. The restricted water molecules within the biofilm are displayed in the light orange to white color range associated with low T_2 values (20 ms to 40 ms), and the free water is displayed as black (60 ms to 65 ms) (Hoskins et al., 1999; Manz et al., 2003; Seymour et al., 2004). Note density variations within the biomass are evident from regions of higher intensity. The biofilm was placed vertically in the magnet 4 h after inoculation and the flow was stopped every 8–10 h for 20 min so that the biofilm growth could be observed via MRI. The first detectable contrast was observed at 24 h. At 24 h the biofilm has formed an approximately 100 μm thick layer of fairly uniform height. The biofilm contains hollowed regions near the capillary wall, several of which are clearly visible slightly left of center at the bottom of the image. At 32 h after inoculation the biofilm thickness is increasing in a somewhat heterogeneous fashion with clusters of greater thickness. By 36 h after inoculation the biofilm exhibits significant tower-like structures and heterogeneity. Calculation of roughness and surface enlargement from such images (Manz et al., 2003) can be made to quantify variation over time. Regions of high molecular mobility, dark, and low molecular mobility, bright, are heterogeneously dispersed throughout the biofilm for times out to 55 h. The data clearly indicate the structural heterogeneity and further study is ongoing to determine if regions of low mobility due to cell clusters can be differentiated from dense EPS regions. An interesting point from the perspective of transport within the biofilm is the fact that what is directly measured is molecular mobility from which biomass presence is inferred. It may be possible to analyze the data from a perspective such as volume averaging and attempt to correlate average material transport properties (Wood et al., 2002) to the measured spatial distribution of molecular mobility.

Advective Transport

Spatially resolved images of the impact of a biofilm on the advection field for three slices across the capillary are presented in Figure 3. The biofilm is primarily located on the wall shown in the slice of Figure 3a. This wall is the capillary bottom relative to gravity during inoculation and since *S. epidermidis* is a non-motile bacterium the cells sediment until contact with a surface where they attach and from there form a biofilm. Figure 3a shows the image of the biofilm structure with areas of biofilm fouling in orange

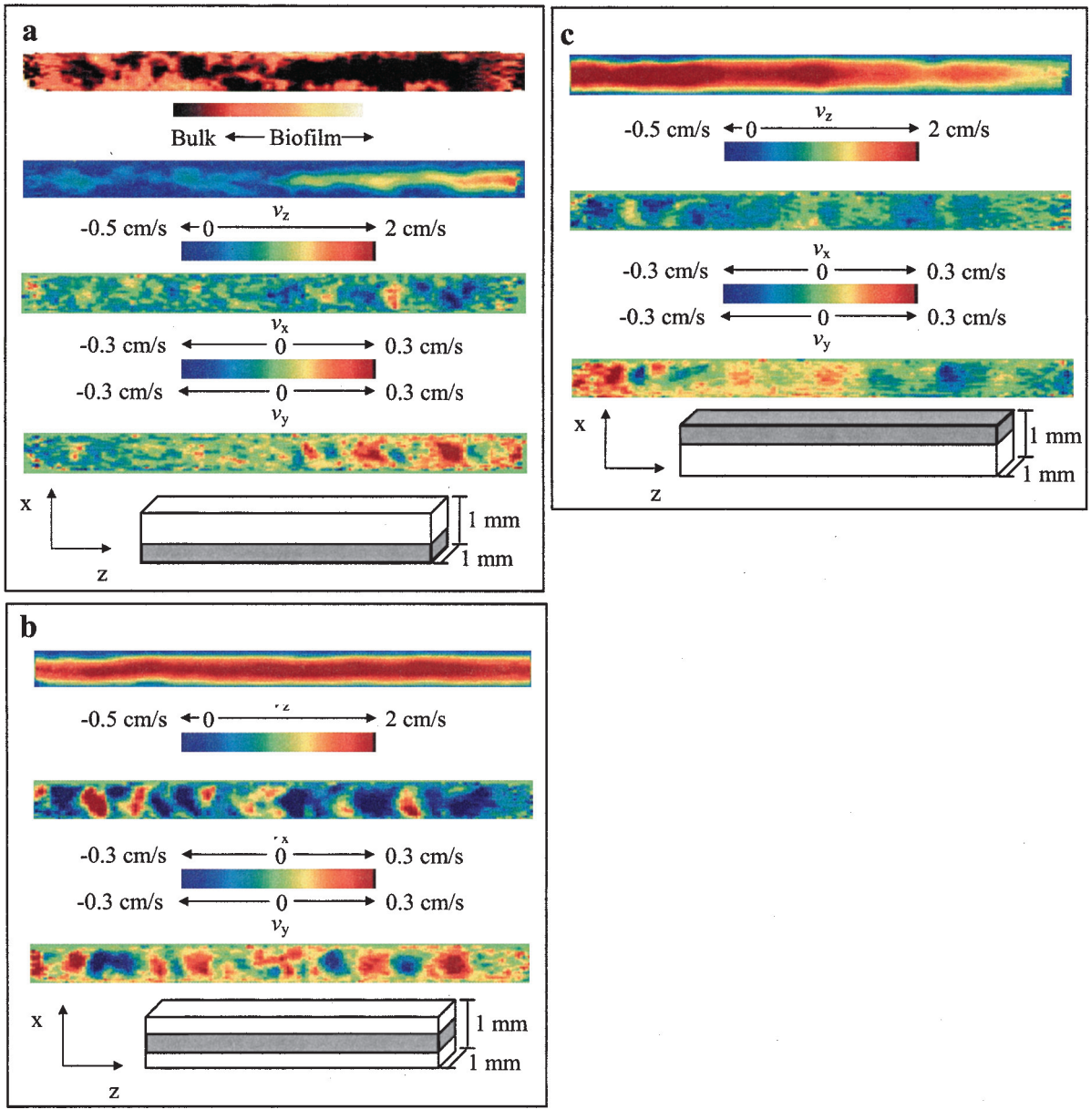

Figure 3. Impact of biofilm growth on the 3D velocity field. For each slice represented by the gray shaded area in the schematic, the corresponding T_2 relaxation map (if biofilm is present), and three velocity maps are shown. In the T_2 map, biofilm is indicated by orange tones, only (a) shows a T_2 map since there was no biofilm present in the other two slices. In the z-component velocity maps (v_z), the main axial component to the right is indicated by red. A positive (red) x-component represents flow up the page and a negative (blue) x-component represents flow down the page. A positive (red) y-component represents flow into the page, a negative (blue) y-component represents flow out of the page. These figures show the flow is affected across the entire capillary by the biofilm.

tones. Note no biomass was detected in the slice of Figure 3b and 3c so T_2 maps are not displayed. The second image from the top in Figure 3a is the z-component of velocity, v_z. The z-direction, as indicated by the axes in the bottom left corner, is the primary flow direction with the largest magnitude of velocity as seen on the color bar below the image. A color of red in the v_z image indicates that the vector component parallel to the z-axis is pointing in the positive z-direction, to the right, with a magnitude of 2 cm/s. The third and fourth images in Figure 3a are of the secondary flow x- and y-components of velocity, v_x and v_y. For v_x, red in the image is for a vector with a magnitude of 0.3 cm/s in the positive x-direction, upwards, while purple in the v_x image is for a vector in the negative x-direction with -0.3 cm/s. Analogously, v_y red is for vectors pointing out of the page with a magnitude of 0.3 cm/s and purple indicates the vector pointing into the page -0.3 cm/s. In a clean capillary, v_z is the only component of velocity present and it is uniform along the length of the capillary in contrast to the biofilm impacted system (Seymour et al., 2004). A comparison of the T_2 map and v_z shows that in areas where biomass is present, v_z drops down to values close to zero as

indicated by blue and purple colors. The secondary components of velocity, v_x and v_y, appear as random noise in areas heavily fouled with biomass while in areas where biofilm is not present, indicated by black in the T_2 map, the secondary components of velocity begin to develop a distinct periodicity.

The velocity components in the middle of the capillary in Figure 3b have the same velocity color bar orientations as Figure 3a. Although there is no biomass in this slice, the flow is none the less, disturbed due to the biofilm on the wall of the capillary in the slice shown in Figure 3a. The z-component of velocity is zero at the walls due to the no-slip boundary and maximum near the center at any point across the width of the capillary. However, along the length of the capillary the velocity profile is nonuniform and non-symmetric, unlike rectilinear flow in a clean capillary. Significant secondary x- and y-components of velocity are present in this slice through the capillary. As discussed above, secondary flows are of particular interest since they alter non-axial transport within a capillary bioreactor from diffusive dominated to advection dominated, changing the fluid mixing within the capillary. The secondary velocity components are periodic on a scale of the capillary cross sectional length. Experiments are currently underway to scale the bioreactor cell and examine the significance of this periodicity with regard to capillary shape and diameter. It is obvious from the measured velocity field the Navier-Stokes equation is now dependent on three spatial dimensions as opposed to one in a clean capillary and complex solutions arise due to the nonlinearity of the problem (Greenburg,

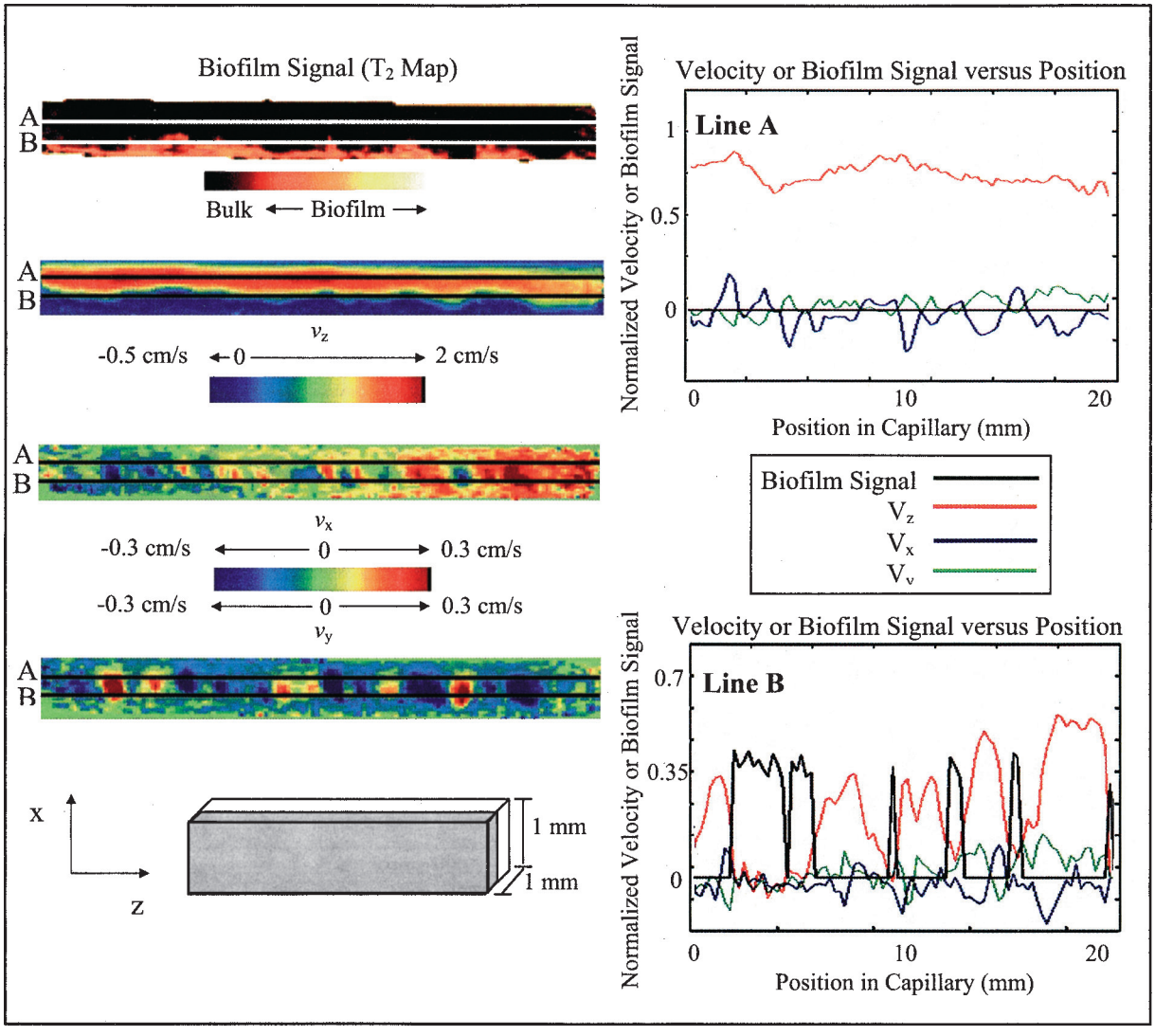

Figure 4. Quantitative data on the correlation of biofilm and velocity for a slice perpendicular to maps in Figure 3. Lines A, in bulk fluid, and B, intersecting biofilm fluid interface, indicate positions along the x-coordinate, that the graphs of biofilm presence and $v_i(x, z)$ shown on the right are plotted for. In areas where biomass is present the biofilm signal indicator, black line, increases from zero to a maximum of 1 at the T_2 map point of highest intensity. The components of velocity are normalized by the maximum axial velocity. Non-axial components of velocity are significant at both heights A and B with maximum non-axial velocity $\approx$ 20% of the axial maximum. In line A the 180° out of phase coupling of v_x, blue line, and v_y, red line can be clearly seen. Line B indicates the strong correlation between the biomass and axial velocity near the interface.

1988) suggesting the applicability of dynamical systems theory (Ottino, 1989). The velocity maps for the slice opposite the biofilm, Figure 3c, show that even at the wall farthest away from the biofilm v_z is impacted. The data indicate that imposition of negligible secondary velocity, $v_x = v_y = 0$ at the top of the bulk fluid, capillary center in our data, as has been done in simulations is an incorrect boundary condition (Picioreanu et al., 2000b). The profile is nonuniform down the length of the capillary, which is explained by accounting for the dynamics of the entire capillary in the context of mass conservation. Comparing the axial velocity images for bottom and top slice it is clear that where v_z is of smaller magnitude, yellow, in Figure 3a it is maximal, red, in the same region of Figure 3c and vice versa. Since the volumetric flow rate is fixed the velocity in the slices above the biomass must increase to ensure mass conservation.

Figure 4 shows data for a slice orientation perpendicular to those of Figure 3 of the same section of the capillary. The cross-sectional depth profile of the biofilm can be seen in the T_2 map for this slice, showing the heterogeneity of the biofilm structure.To quantify some of the visual observations from Figure 3 quantitative velocity data, $v_i(x, z)$, is plotted as a function of the axial direction for various positions x. The lines A and B drawn through the images indicate the x position of the data presented in the graphs to the right and are chosen in the bulk fluid and at the biofilm–fluid interface. To construct a biofilm indicator function the T_2 data are masked, setting values associated with free water equal to zero and normalized by the maximum T_2 value. This allows the biofilm signal to be displayed as a value above zero where biomass is present, with 1 the maximum within the image, and zero in areas with no biomass. All three components of velocity are normalized by the maximum z-direction velocity so that the x- and y-components are displayed as a percentage of the axial velocity and are indicative of the mixing intensity (Ottino, 1989).

Data for the bulk fluid, line A, indicate v_z varies as a function of z but maintains a value near 0.75 of maximum velocity. The periodicity of v_x and v_y is clearly evident in the graph of line A and a 180° out of phase coupling of the components is seen with one positive when the other is negative. The secondary flow components are 0.1 to 0.2 of the maximum axial velocity and spatially oscillatory. The significant non-axial velocities indicate non-axial mass transport has gone from diffusion dominated, $Pe_l = 0$, in the clean capillary, to advection dominated, $Pe_l \sim 2 \times 10^3$, due to the impact of the biofilm. For comparison, the axial Peclet number is $Pe_L \sim 2 \times 10^5$. Line B intersects areas covered by biomass and areas of only bulk fluid as indicated in the graph of the biofilm signal. Comparing the T_2 map and the graph, line B is seen to intersect a large biofilm clump from an axial position of 3 mm to 7 mm at a depth approximately 120 μm below the biofilm–fluid interface and is near the biofilm surface along the entire observed length. This graph quantifies the visual observation from Figure 3 that in areas where there is biomass, indicated by a value above zero on the black line, v_z, indicated by the red line, drops down to values less than 0.1 of maximum. Indeed, the axial velocity is negative at sufficient depth within the biomass as in the region from 3 mm to 7 mm, as is evidenced by the axial velocity image with regions of small negative velocity within the biofilm. Negative velocities have been demonstrated in simulations (Picioreanu et al., 2000b) and intimated in lower resolution MRI experiments (Lewandowski et al., 1994) and may provide the mechanism by which upstream biofilm colonization can occur. The secondary velocity components v_x, green line and v_y, blue line, are small within the biofilm, and while not quite as regular as in line A, exhibit an out-of-phase spatial oscillation and obtain amplitudes up to 0.1 of maximum axial velocity. The spatial variations in the velocity field are significant over mm scales along the biofilm. The rapid changes in the secondary flow velocities indicate they generate shear stresses, which may be important in regions where the axial velocity is more constant.

The correlation between biofilm and axial velocity is presented in Figure 5. The graph plots the normalized axial velocity as a function of the normalized T_2 signal intensity. Smaller normalized T_2 values indicate shorter relaxation times that are from biofilm-bound water, which covers a range from approximately 0.3 to 0.5 on the abscissa, while more mobile bulk water has longer T_2 relaxation times that are indicated by normalized values of 0.5 to 0.65. The ordinate is the normalized axial velocity computed by dividing v_z at each point by the maximum value for the slice.

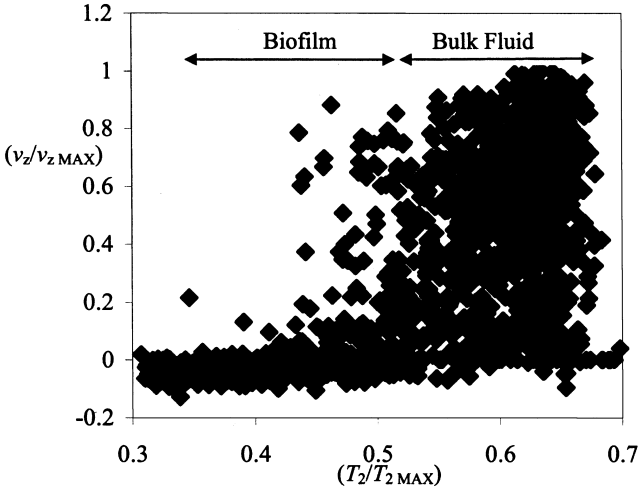

Figure 5. Correlation between axial velocity and biomass given by normalized T_2 value vs. normalized axial velocity. In areas where biomass is present, indicated by low T_2 values, v_z drops predominately to zero or negative values. In areas in the bulk fluid, indicated by longer T_2 relaxation times, a full range of values for v_z exist. This range of v_z values goes from zero at the walls, due to the no-slip boundary, and out to the maximum value ($v_z/v_{z,\max}$) = 1 at the center of the capillary. Negative velocity values in the bulk fluid are due to vortices. This data is for the slice of data shown in Figure 4 and T_2 values are normalized by the maximum T_2 value for this slice as is v_z.

The graph is for all the data points in the slice of the capillary in Figure 4 and so provides a statistical characterization of the trends in the quantitative velocity profiles. From the graph the obvious trend is that in areas where biofilm is present, v_z is near to zero with a trend toward negative values. In contrast, the bulk fluid has some negative v_z data points, due to vortices, and covers the full range of velocities from zero, at the walls of the capillary, to the maximum, $v_z/v_{z,\,max} = 1$, at the center. The indication of negative velocities has been suggested to be due to vortex flow within valleys (Picioreanu et al., 2000b) and are indicated by the negative velocities associated with the bulk fluid but would not seem to account for the negative velocity trend within the biofilm biomass.

The structure of the advection field indicated by the data is that of a strongly perturbed helical flow. This is evidenced by velocity maps measured for consecutive slices perpendicular to the flow shown in Figure 6. The axial velocities again indicate higher maxima when the cross-section occupied by the flow are smaller, as in slice 1 and 2 relative to slices 3, 4, and 5, in agreement with mass conservation for fixed volumetric flow rate of an incompressible fluid. Of greatest interest here are the secondary flow components. Note the onset of a vortex from slices 1 and 2 to a fully developed clockwise vortex flow in slice 3. In slice 4 and 5 the coherent vortex structure is rotated and decaying with axial position. It is important to remember that the velocity measured is for a displacement time Δ of 7 ms, but time averaging over the image acquisition time of 10 minutes occurs due to encoding of information in each acquired signal so the spatial distribution velocity components measured are stationary (Li et al., 1994). This is clear visualization of the complex spatial distribution of flow structures, which generates a corresponding variation in mass transport as demonstrated in simulations (Picioreanu et al., 2000b). Recent simulations of the structure of secondary flows, Dean vortices, in curved microchannels suggest that "switching" between flow patterns with a varying number of vortices during axial transit generates a chaotic flow and impacts mixing (Schonfeld and Hardt, 2004). Figure 6 indicates a "switching" type event with strong negative v_x, blue, and positive v_y, red, components in slice 1 and 2, transitioning to the coherent vortex in slice 3 and an inverted configuration in slices 4 and 5 relative to the

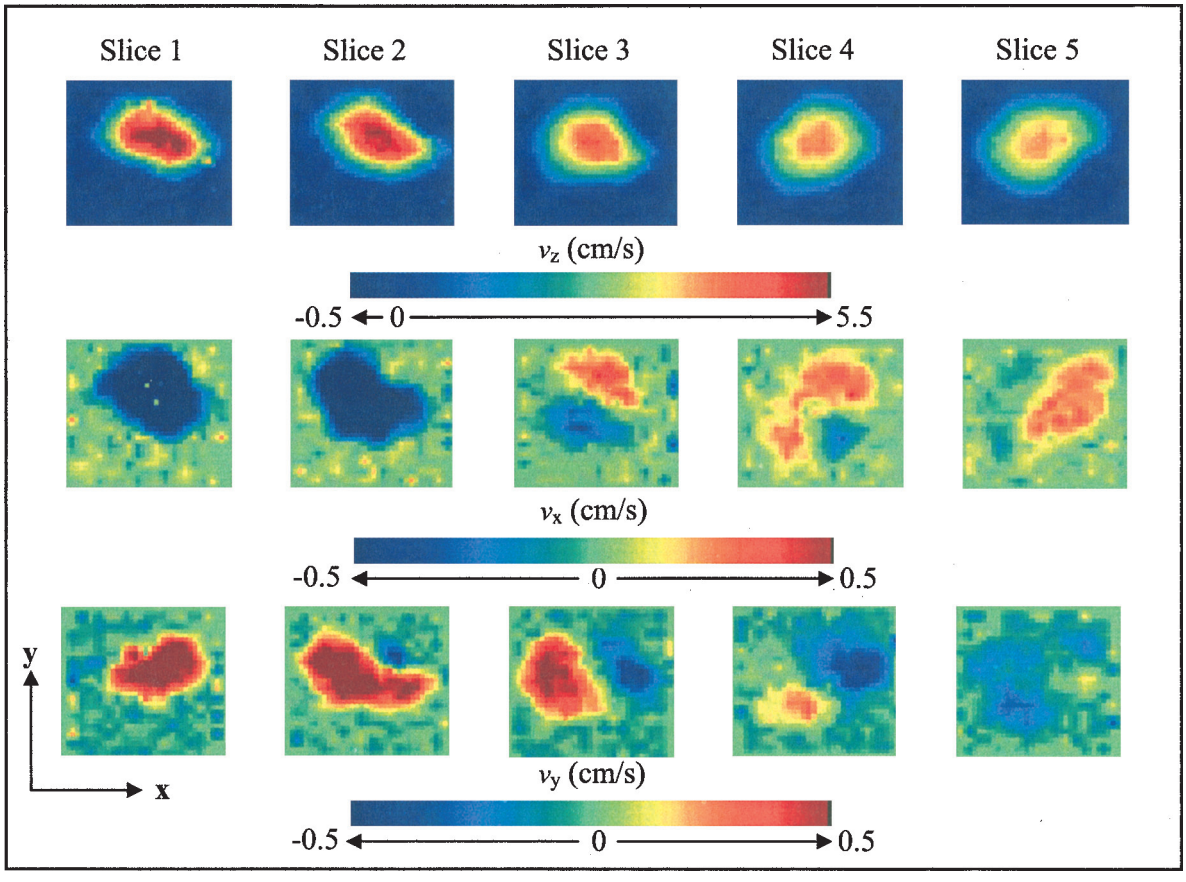

Figure 6. These images display the three components of velocity in five consecutive slices through the transverse cross-section of the capillary. The direction of bulk flow is from slice 1 to 5 with each slice 300 μm thick and contiguous, positive axial velocity, red, out of the page. A negative (blue) *x*-component represents flow to the left while a positive (red) *x*-component represents flow to the right. A negative (blue) *y*-component represents flow down the page while a positive (red) *y*-component represents flow up the page. The helical nature of the flow is clear with non-axial flow changing directions through the sequence of slices and going through a coherent clockwise vortex flow in slice 3.

flow upstream of slice 3, with positive v_x, red, and negative v_y, blue.

Residence Time Distribution

The quantification of industrial systems with complex flow such as packed- and fluidized-bed reactors is often accomplished using the residence time distribution since it indicates when flow pathologies such as channeling occur (Fogler, 1986). Figure 7 shows the propagator of the motion measured for a clean and a biofilm-impacted capillary (Seymour et al., 2004) and the residence time distributions calculated for each. The clean capillary gives an experimental propagator equal to the theoretical velocity distribution convolved with a Gaussian diffusion curve (Seymour et al., 2004). For the flow around the biofilm structure note the appearance of a high velocity tail indicating higher probability of large displacements relative to the clean capillary. The slow flow peak near zero displacement results from the protons trapped within the EPS gel matrix where the primary transport mechanism is diffusive. The residence time distribution integrated over time $\int_0^t N(L,t)dt$ gives the fraction of fluid which has been in a reactor of length L for less than time t. In Figure 7 L is the average length traveled by the fluid in the time Δ = 15 ms, i.e., $L = v_{z,\ \mathrm{avg}}\ \Delta$. The long tail in the biofilm propagator manifests itself as a feature at short residence times, whereas the large zero displacement peak in the biofilm propagator manifests itself as a long tail on the RTD. The presence of flow structures which generate significant trapping of fluid particles, as is found in cellular vortex flows like Rayleigh-Benard convection (Bouchaud and Georges, 1990), manifest themselves as peaks in the RTD (Mezic et al., 1999) and are not indicated by the data.

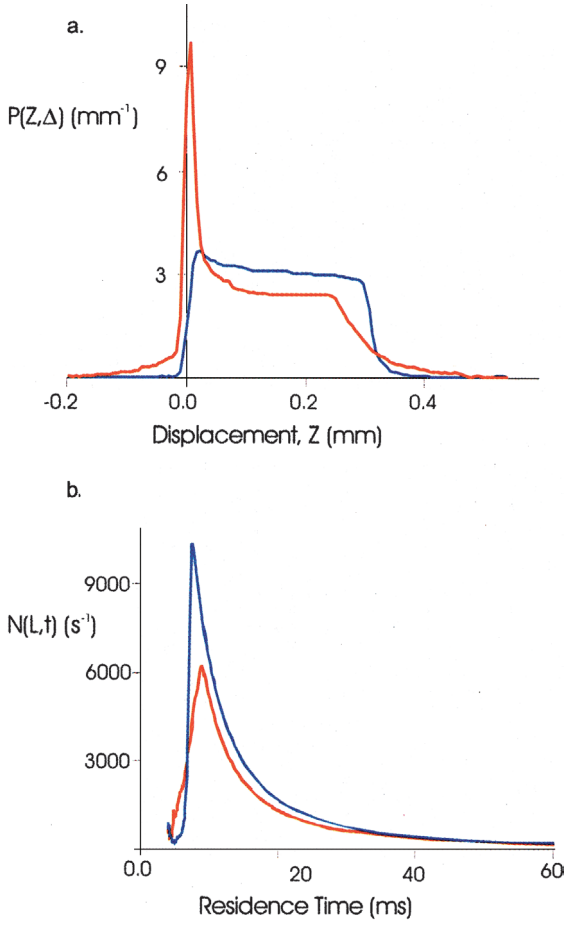

Figure 7. (a) Propagators in both a clean square capillary (blue) and for flow around biofilm structure (red) for an observation time, Δ = 15 ms (Seymour et al., 2004). (b) Residence time distribution functions calculated from the propagator data shown in a.

CONCLUSIONS

Magnetic resonance microscopy methods have been demonstrated to provide data on the advective transport in capillary bioreactors, which provides the extension of conceptual models of mass transport. Non-axial advection components up to 20% of the maximum axial velocity are measured, corresponding to a non-axial Peclet number of 2000. The presence of significant secondary flows such as these require modification of mass transfer coefficient approaches to model the transport of mass from the bulk fluid to the biofilm. The spatial variation of the secondary flows in the axial direction is oscillatory and the orthogonal components tend to be out of phase. The data show general agreement with simulations in the presence of negative axial velocities in regions of the heterogeneous biofilm structure and spatial variation of mass transfer based on the secondary flow (Picioreanu et al., 2000b). The overall flow is helical in nature and flow structures such as coherent vortices develop and decay along the axis of flow. The biofilm impact on reactor behavior is quantified to some extent by the RTD and indicates a portion of fluid spends less time in the capillary relative to a clean system; a persistent tail of the RTD is generated by the fluid within the EPS. The data indicate that concepts from dynamical systems theory that have been broadly applied to study mixing in complex flows generated in mixing devices (Ottino, 1989) may provide a means for greater quantification of the interaction between the bulk fluid motion and mass transport in biofilm reactor systems. The ability to incorporate microscale advection data into macroscale mass transfer models has the potential to impact the design of microfluidic-based bioreactor systems (Stone and Kim, 2001) where the spatial variability of the flow field controls bioactivity (Takayama et al., 1999).

NOMENCLATURE

c	mass concentration	(kg m^{-3})
D	diffusion coefficient	(m^2 s^{-1})
$\mathbf{D}$	diffusion tensor	(m^2 s^{-1})
E	MR spin echo function, normalized voltage response	

g_i	magnetic field gradient for motion sensitivity	(T m^{-1})
G_i	magnetic field gradient in direction i	(T m^{-1})
J	mass flux	(kg m^{-2}s^{-1})
k_i $i = x, y, z$	MR Fourier reciprocal wavelength to space	k_i = (m^{-1})
k_c	mass transfer coefficient	(m s^{-1})
l	characteristic non-axial capillary length scale	(m)
L	axial length of capillary	(m)
N	residence time distribution function	(s^{-1})
p	pressure	(Pa)
$\bar{P}$	averaged propagator, or conditional probability distribution function	(m^{-1})
Pe	Peclet number	$Pe = v_{z,\,\max}\, l/D = Re\, Sc$
Pe_L	Peclet number based on axial length and velocity	$Pe_L = v_{z,\,\max}\, L/D = Pe\, L/l$
Pe_l	Peclet number based on non-axial length and velocity	$Pe_l = v_{x(y),\,\max}\, l/D$
q	MR Fourier reciprocal wavelength to displacement q	(m^{-1})
Re	Reynolds number	$Re = v_{z,\,\max}\, l/\nu$
s	MR slice thickness	(m)
S	MR signal	(V)
Sc	Schmidt number	$Sc = \nu/D$
Sh	Sherwood number	$Sh = k_c\, l/D$
T_2	transverse, spin-spin relaxation time	(s)
t_e	MR pulse sequence echo time	(s)
v_i $i = x, y, z$	component of velocity	(m/s)
$\mathbf{v}$	velocity vector	(m/s)
x	Cartesian spatial coordinate	
y	Cartesian spatial coordinate	
z	Cartesian spatial coordinate, aligned with capillary axis	
Z	displacement, $Z = z\text{-}z'$, aligned with capillary axis	(m)
∇	vector differential operator	(m^{-1})

Greek Letters

δ	duration of velocity encoding gradient pulses	(s)
Δ	observation time for encoding displacement	(s)
γ	gyromagnetic ratio, for protons γ =2.675e8	(rad s^{-1} T^{-1})
ν	kinematic viscosity	(m^2 s^{-1})
τ_i	duration of spatial encoding gradient in direction i	(T m^{-1})
ρ	spin density, density of MR active nuclei	(kg m^{-3})

Subscripts

avg	average
bulk	bulk fluid
max	maximum
x	Cartesian spatial coordinate
y	Cartesian spatial coordinate
z	Cartesian spatial coordinate, aligned with capillary axis

References

Batchelor GK. 1967. An introduction to fluid dynamics. Cambridge: Cambridge University Press.

Beyenal H, Lewandowski Z. 2002. Internal and external mass transfer in biofilms grown at various flow velocities. Biotechnol Prog 18:55–61.

Bird RB, Stewart WE, Lightfoot EN. 2002. Transport phenomena. New York: John Wiley & Sons. 780 p.

Bouchaud J-P, Georges A. 1990. Anomalous diffusion in disordered media: Statistical mechanisms, models and applications. Phys Rep 195(4&5):127–293.

Callaghan PT. 1991. Principles of nuclear magnetic resonance microscopy. New York: Oxford University Press.

Callaghan PT, Codd SL, Seymour JD. 1999. Spatial coherence phenomena arising from translational spin motion in gradient spin echo experiments. Concepts Magn Res 11:181–202.

Costerton JW, Stewart PS, Greenberg E. 1999. Bacterial biofilms: A common cause of persistent infections. Science 284:1318–1322.

de Beer D, Stoodley P, Lewandowski Z. 1994. Liquid flow in heterogeneous biofilms. Biotechnol Bioeng 44:636–641.

Eberl HJ, Picioreanu C, Heijnen JJ, van Loosdrecht MCM. 2000. A three-dimensional numerical study on the correlation of spatial structure, hydrodynamic conditions, and mass transfer and conversion in biofilms. Chem Eng Sci 55:6209–6222.

Edzes HT, van Dusschoten D, van As H. 1998. Quantitative T_2 imaging of plant tissues by means of multi-echo MRI microscopy. Magn Res Imag 16(2):185–196.

Fogler HS. 1986. Elements of chemical reaction engineering. Englewood Cliffs, NJ: Prentice Hall.

Garroway AN. 1974. Velocity measurements in flowing fluids by NMR. J Phys D: Appl Phys 7:L159–L163.

Greenburg MD. 1988. Advanced engineering mathematics. Englewood Cliffs, NJ: Prentice Hall.

Horn H, Hempel DC. 1997. Substrate utilization and mass transfer in an autotrophic biofilm system: Experimental results and numerical solution. Biotechnol Bioeng 53(4):363–371.

Hoskins BC, Fevang L, Majors PD, Sharma MM, Georgiou G. 1999. Selective imaging of biofilms in porous media by NMR relaxation. J Magn Res 139:67–73.

Hyde J, Darouiche R, Costerton JW. 1998. Strategies for prophylaxis against prosthetic valve endocarditis: A review article. J Heart Valve Dis 7: 317–326.

Lewandowski Z, Altobelli SA, Majors PD, Fukushima E. 1992. NMR imaging of hydrodynamics near microbially colonized surfaces. Water Sci Technol 26(3–4):577–584.

Lewandowski Z, Beyenal H. 2003. Mass transport in heterogeneous biofilms. In: Wuertz S, Bishop PL, Wilderer PA, editors. Biofilms in wastewater treatment. London: IWA Publishing. p 147–177.

Lewandowski Z, Stoodley P, Altobelli SA, Fukushima E. 1994. NMR imaging of hydrodynamics near microbially colonized surfaces. Water Sci Technol 26(3–4):577–584.

Li T-Q, Seymour JD, Powell RL, McCarthy KL, Odberg L, McCarthy MJ. 1994. Turbulent flow studied by time averaged NMR imaging: Measurements of velocity profile and turbulent intensity. Magn Res Imag 12(6):923–934.

Lichtenberg AJ, Lieberman MA. 1992. Regular and chaotic dynamics. New York: Springer-Verlag.

Manz B, Volke F, Goll D, Horn H. 2003. Measuring local flow velocities and biofilm structure in biofilm systems with magnetic resonance imaging (MRI). Biotechnol Bioeng 84(4):424–432.

Mezic I, Wiggins S, Betz D. 1999. Residence time distributions for chaotic flows in pipes. Chaos 9(1):173–182.

Ottino JM. 1989. The kinematics of mixing: Stretching, chaos and transport. Cambridge: Cambridge University Press.

Ottino JM. 1990. Mixing, chaotic advection and turbulence. Annu Rev Fluid Mech 22:207–254.

Picioreanu C, van Loosdrecht MCM, Heijnen JJ. 2000a. Effect of diffusive and convective substrate transport on biofilm structure formation: A two dimensional modeling study. Biotechnol Bioeng 69(5): 504–515.

Picioreanu C, van Loosdrecht MCM, Heijnen JJ. 2000b. A theoretical study on the effect of surface roughness on mass transport and transformation in biofilms. Biotechnol Bioeng 68(4):355–369.

Schonfeld F, Hardt S. 2004. Simulation of helical flows in microchannels. AIChE J 50(4):771–778.

Seymour JD, Codd SL, Gjersing EL, Stewart PS. 2004. Magnetic resonance microscopy of biofilm structure and impact on transport in a capillary bioreactor. J Magn Res 167:322–327.

Stewart PS, Costerton JW. 2001. Antibiotic resistance of bacteria in biofilms. The Lancet 358:135–138.

Stone HA, Kim S. 2001. Microfluidics: Basic issues, applications and challenges. AIChE J 47(6):1250–1254.

Stoodley P, de Beer D, Lewandowski Z. 1994. Liquid flow in biofilm systems. Appl Environ Microbiol 60(8):2711–2716.

Stoodley P, Dodds I, Boyle JD, Lappin-Scott HM. 1999a. Influence of hydrodynamics and nutrients on biofilm structure. J Appl Microbio Symposium Supplement 85:19S–28S.

Stoodley P, Lewandowski Z, Boyle JD, Lappin-Scott HM. 1999b. Structural deformation of bacterial biofilms caused by short-term fluctuations in fluid shear: An in situ investigation of biofilm rheology. Biotechnol Bioeng 65(1):83–92.

Stoodley P, Yang S, Lappin-Scott HM, Lewandowski Z. 1997. Relationship between mass transfer coefficient and liquid flow velocity in heterogeneous biofilms using microelectrodes and confocal microscopy. Biotechnol Bioeng 56:681–688.

Takayama S, McDonald JC, Ostuni E, Liang ML, Kenis PAJ, Ismagilov RF, Whitesides GM. 1999. Patterning cells and their environments using multiple laminar fluid flows in capillary networks. Proc Natl Acad Sci 96:5545–5548.

van As H, Lens P. 2001. Use of 1H NMR to study transport processes in porous biosystems. J Industr Microbiol Biotechnol 26:43–52.

Wood BD, Quintard M, Whitaker S. 2002. Calculation of effective diffusivities for biofilms and tissues. Biotechnol Bioeng 77(5):495–516.

Xia F, Beyenal H, Lewandowski Z. 1998. An electrochemical technique to measure local flow velocity in biofilms. Water Res Res 32(3631–3636):55–61.